nature chemistry

ARTICLES

https://doi.org/10.1038/s41557-021-00827-7

Check for updates

Electron spin resonance of single iron phthalocyanine molecules and role of their non-localized spins in magnetic interactions

Xue Zhang[1,2], Christoph Wolf[1,2], Yu Wang[1,2], Hervé Aubin[3], Tobias Bilgeri[4], Philip Willke[1,2,5], Andreas J. Heinrich[1,6] ✉ and Taeyoung Choi[1,6] ✉

Electron spin resonance (ESR) spectroscopy is a crucial tool, through spin labelling, in investigations of the chemical structure of materials and of the electronic structure of materials associated with unpaired spins. ESR spectra measured in molecular systems, however, are established on large ensembles of spins and usually require a complicated structural analysis. Recently, the combination of scanning tunnelling microscopy with ESR has proved to be a powerful tool to image and coherently control individual atomic spins on surfaces. Here we extend this technique to single coordination complexes—iron phthalocyanines (FePc)—and investigate the magnetic interactions between their molecular spin with either another molecular spin (in FePc–FePc dimers) or an atomic spin (in FePc–Ti pairs). We show that the molecular spin density of FePc is both localized at the central Fe atom and also distributed to the ligands (Pc), which yields a strongly molecular-geometry-dependent exchange coupling.

Chemical engineering and fabrication of single molecular spins is of vital importance in molecule-based quantum devices[1]. There are various approaches to detect and control single molecular spins, such as the optical detection of diluted molecular spins[2–4], magnetic resonance force microscopy[5], nitrogen-vacancy magnetometry[6] and break-junction-based molecular devices[7–9]. Nevertheless, these systems typically require embedding the molecule in a solid-state host and lack the flexibility to locate and access individual spins or harness intra- and intermolecular spin–spin interactions.

Conventional electron spin resonance (ESR) studies on chemical ensembles[10,11] are a very useful tool to elucidate the chemical structures at the molecular level, but they rely on the order of ~10^{10} spins and often require complementary analysis techniques or theoretical calculations. The recent development of scanning tunnelling microscopy (STM) combined with ESR provides the advantage to investigate single molecular spins with atomic resolution. ESR–STM introduces a radio frequency electric field at the tunnelling junction, which can coherently drive individual atomic spins on surfaces[12–14]. The change in spin state is read out by a spin-polarized tip through tunnelling magnetoresistance. This combined ESR–STM approach enables a precise atom manipulation and imaging in subnanometre scale with a submicroelectronvolt (~10 MHz) energy resolution. Previous ESR–STM studies focused on the spins of single transition metal adatoms[12,14–16] rather than those of single molecules, other than early attempts on the organic molecule α,γ-bisdiphenylene β-phenylallyl at room temperature and in ambient conditions[17]. Coordination compounds, in particular, often have non-trivial spin distribution owing to the ligands[18], which gives a unique opportunity to tune the spin distribution on the ligands to engineer a spin–spin interaction with atomic resolution.

Metal phthalocyanines with various substitutional central metal atoms have been extensively employed as model systems in many-body quantum physics[18,19] and spin-dependent transport[20]. Here we explore a system of spin-1/2 iron phthalocyanine (FePc) molecules, iron (Fe) atoms and titanium (Ti) atoms adsorbed on a bilayer magnesium oxide (MgO), itself grown atop a Ag(100) surface. We performed ESR on individual FePc molecules and characterized the effects of Pc ligand orientations on the spin–spin interactions in FePc–FePc dimers and FePc–Ti pairs. This enabled us to visualize the electronic configuration of molecular orbitals and characterize the role of the ligands using nearby atoms as sensors to measure the magnetic dipolar and exchange coupling between the molecular spin and ESR-active species (FePc and Ti). Density functional theory (DFT) calculations, in good agreement with the experimental results, suggest that the spin density of the compound mainly located on the Fe centre spreads to the Pc ligands. These findings highlight the role of non-localized spins in the transfer of magnetic interactions, which can be crucial to fabricate molecular devices[21].

Results and discussion

Single-molecule ESR. Individual FePc molecules, Fe atoms and Ti atoms were deposited in a stepwise manner onto a bilayer (two monolayers (MLs)) MgO surface on a Ag(100) substrate and all the measurements were performed at a temperature of 2 K in a commercial STM with vector magnetic fields. The molecules and atoms were well isolated from each other at a low coverage and were distinguished readily by their topographical appearance, as shown in Fig. 1a. Individual FePc molecules appear as a cross-like shape and lattice analysis indicated that the central Fe atom of the FePc molecule sits atop an oxygen atom of MgO. The molecular axes were rotated by approximately 27° with respect to the underlying oxygen rows (inset of Fig. 1a). The Ti atoms in our experiment were mainly found on oxygen–oxygen bridge sites (marked as Ti_B) and appeared taller than the Fe atoms atop the oxygen site[22,23].

[1]Center for Quantum Nanoscience, Institute for Basic Science (IBS), Seoul, Republic of Korea. [2]Ewha Womans University, Seoul, Republic of Korea. [3]Universités Paris-Saclay, CNRS, Centre de Nanosciences et de Nanotechnologies, Palaiseau, France. [4]Institute of Physics, École Polytechnique Fédérale de Lausanne, Lausanne, Switzerland. [5]Physikalisches Institut, Karlsruhe Institute of Technology, Karlsruhe, Germany. [6]Department of Physics, Ewha Womans University, Seoul, Republic of Korea. ✉e-mail: heinrich.andreas@qns.science; choi.taeyoung@qns.science

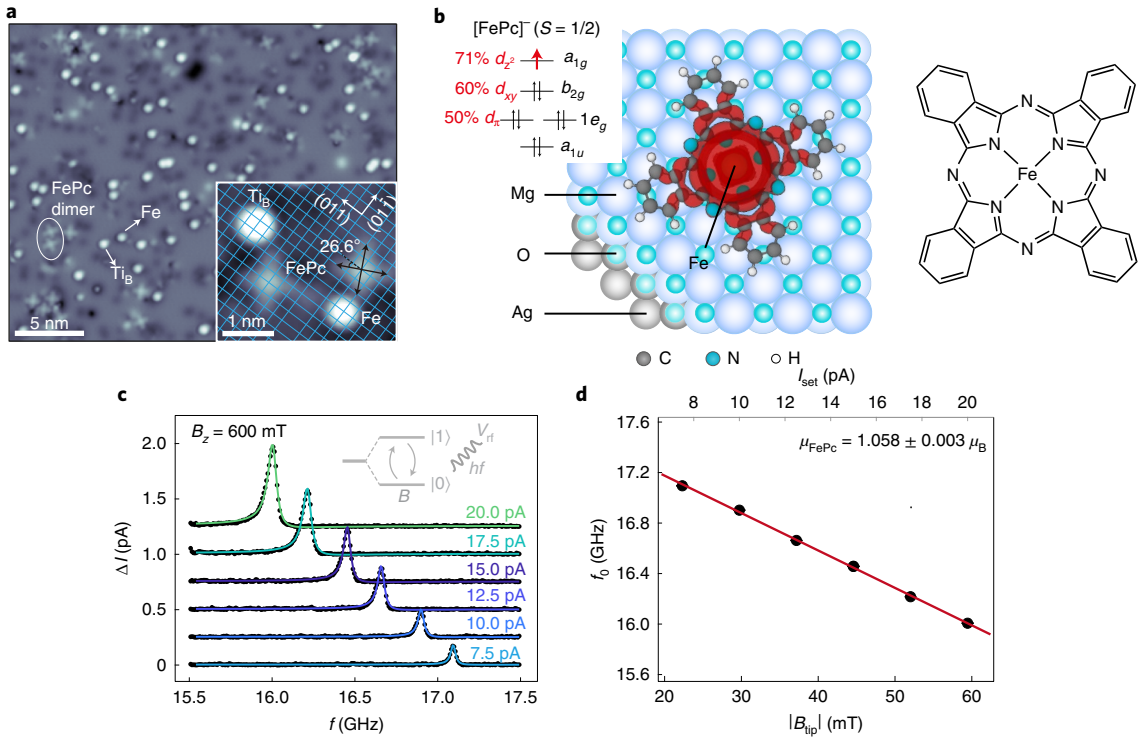

Fig. 1 | [FePc]⁻ molecules adsorbed on MgO/Ag(100) and ESR measurements with varied tip fields. a, STM images of [FePc]⁻ molecules (light grey crosses), Fe (smaller white dots) and Ti_8 (larger white dots) atoms adsorbed on the MgO surface (dark grey background). A naturally formed [FePc]⁻–[FePc]⁻ dimer is circled in white. Inset: magnified view of [FePc]⁻ molecules and Fe and Ti_8 atoms. The blue grid indicates oxygen sites of the underlying MgO surface. Black arrows describe the molecular axes that point to the benzene rings and show an azimuthal angle of 26.6° with respect to the oxygen rows. Scanning conditions: $V = 200$ mV, $I_{set} = 12$ pA for the main image and $I_{set} = 10$ pA for the inset. **b**, Left: isosurface representation (in red) of the frontier orbital (isovalue, 10^{-5}) of a [FePc]⁻ molecule adsorbed on a MgO/Ag(100) surface, which corresponds to the molecular frontier orbital (a_{1g} in the inset). Inset: electron occupancy and *d*-orbital components (%) of the molecular frontier orbitals, $d_\pi = 0.5(d_{zx} + d_{zy})$. Notably, the a_{1u} orbital has no contribution from the *d* component. Right: structure of the FePc complex, which becomes negatively charged when adsorbed atop the MgO surface. **c**, ESR spectra of an individual [FePc]⁻ molecule measured at different tunnelling currents. ESR conditions: $V = 100$ mV, $V_{rf} = 10$ mV. Each spectrum is shifted vertically from one another by 0.75 pA for clarity. Coloured lines are Lorentzian fits of raw ESR spectra (black dots). Inset: schematic representation of controlling the ESR in a two-level system with a radio frequency electric field. **d**, Linear fit (red line) of resonance frequencies obtained from **c** as a function of B_{tip} (I_{set}), which shows the possibility of tuning a local field by the tip. The error bars are smaller than the size of the data dots, and thus not distinguishable. The errors shown in **d** originate from the 95% confidence intervals of the non-linear fits. Source data in ref. [37].

Previous studies reported that FePc possesses a spin $S = 1$ in bulk and on several surfaces[18,24]. Surprisingly, our differential conductance (d*I*/d*V*) spectra measured on well-isolated FePc molecules on a MgO surface showed a clear conductance maximum, reminiscent of the Kondo effect at zero bias when no magnetic field is applied, which suggests the FePc spin is $S = 1/2$ (Supplementary Fig. 1). This agrees with our DFT calculations, which suggest that an electron is transferred from the Ag substrate to the adsorbed FePc and the molecular spin becomes $S = 1/2$. The spin density of a negatively charged FePc (referred to as [FePc]⁻ in the rest of the discussion) is plotted in Fig. 1b, and indicates that the spin distributes mainly on the central Fe atom and partially extends along the Pc ligands[19]. Further analysis of the frontier orbital indicates that it consists of about 71% dz^2 and 29% contributions from the ligands and other orbitals (Supplementary Sections 8, 10 and 11).

We performed ESR on individual [FePc]⁻ molecules using radio frequency sweeps[12,14] at a fixed external magnetic field (Fig. 1c). The external magnetic field sets the Zeeman splitting of the [FePc]⁻ spin and the two Zeeman states of [FePc]⁻ spin (labelled as |0> and |1>, inset of Fig. 1c) can be coherently driven when the frequency of the applied oscillating electric field V_{rf} matches the Larmor frequency, which is known as the angular frequency of the spin processing around the external magnetic field axis. The spin Hamiltonian of a single [FePc]⁻ spin system can be written as:

$$H_0 = 2\mu_{\mathrm{FePc}}\mathbf{B}\cdot\mathbf{S}. \quad (1)$$

where μ_{FePc} is the magnetic moment of FePc, **S** is the spin operator and the total magnetic field **B**, which sets the Zeeman splitting, is a sum of external magnetic field ($\mathbf{B}_{ex}$) and tip field ($\mathbf{B}_{tip}$): $\mathbf{B} = \mathbf{B}_{ex} + \mathbf{B}_{tip}$. When we applied an external magnetic field along the out-of-plane (*z*) direction, we simplified the external magnetic field and tip field as B_z and B_{tip}. The resonance frequency f_0 that corresponds to the transition between |0> and |1> states is determined by:

$$hf_0 = 2\mu_{\mathrm{FePc}}(B_z + B_{\mathrm{tip}}). \quad (2)$$

Here, *h* is Planck's constant. The continuous-wave ESR signal can be detected when the ESR driving Rabi time is comparable with a geometric mean of spin relaxation (T_1) and spin coherence time (T_2) (ref. [25]) (Supplementary Section 15). Here, Rabi time describes the half-cycle time needed by a two-level quantum system to perform a cyclic behaviour between the two quantum levels and is determined by $T_{\mathrm{Rabi}} = \frac{1}{\Omega} \propto \frac{1}{V_{\mathrm{rf}}\langle 1|S_x|0\rangle}$, where Ω is the Rabi rate. Although the timescales of T_1 and T_2 are given by the system, an optimal selection of the frequency range and V_{rf}, in principle, can allow the measurement of the ESR signal on other spin systems. Therefore, the ESR–STM method can be applied to other atomic and molecular systems as long as the above condition ($T_{\mathrm{Rabi}} \propto T_1, T_2$) is satisfied. Here we

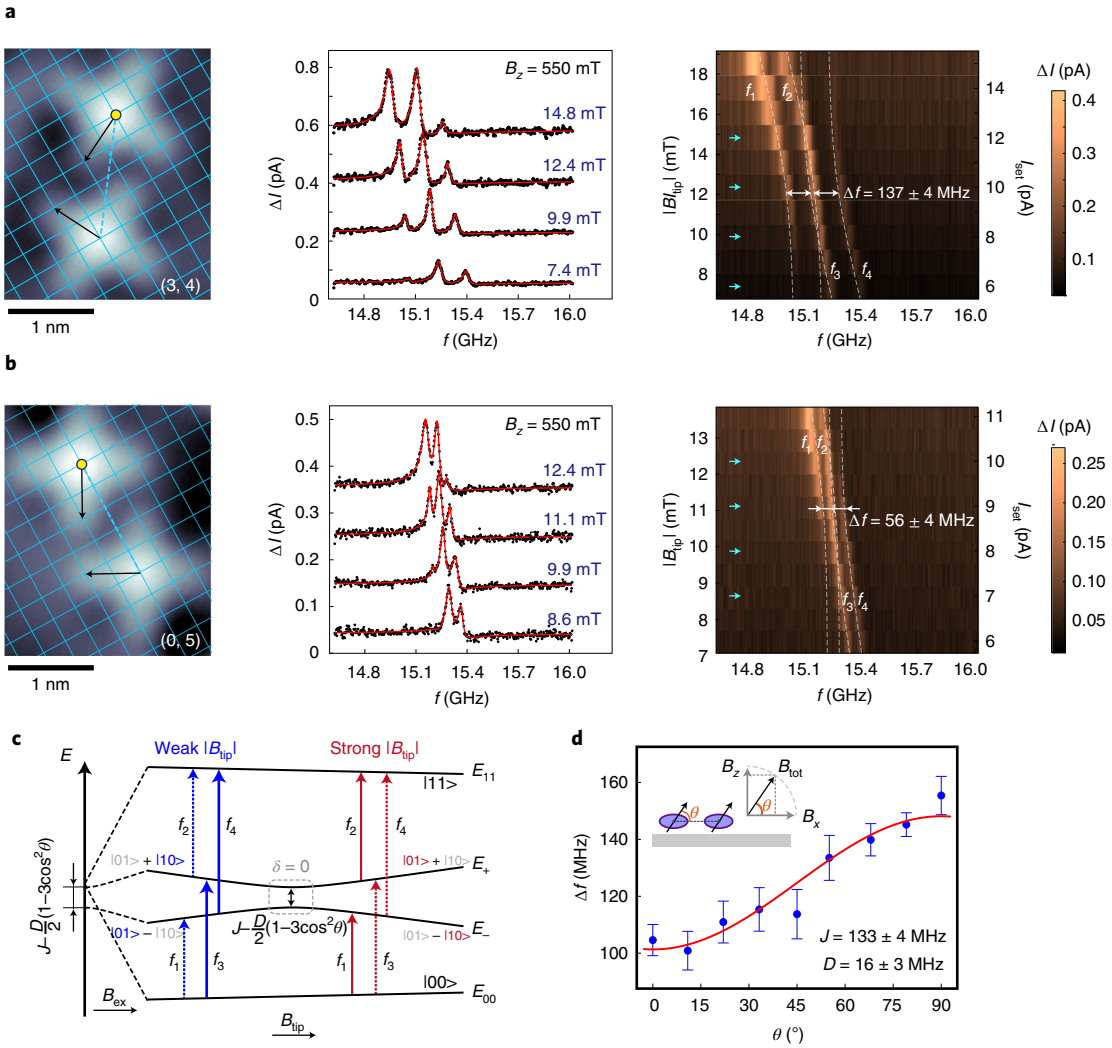

Fig. 2 | Spin coupling in [FePc]$^-$–[FePc]$^-$ dimers. a,**b**, Dimers in configuration (3, 4) (**a**) and (0, 5) (**b**). Left: STM images showing that the (3, 4) and (0, 5) dimers have the same centre–centre distance (dashed lines). Scanning conditions: V = 180 mV, I_{set} = 20 pA. The blue grids indicate the oxygen sites of the underlying MgO surface. Centre: representative ESR spectra of the upper [FePc]$^-$ measured at the yellow dots in the respective left panels. Right: ESR spectra plotted in a colour scale measured at different B_{tip} (I_{set}), showing clearly the difference in the coupling energy (that is, Δf) of (3, 4) and (0, 5) dimers. Blue arrows indicate each ESR spectrum presented in the centre panels. The dotted white curves represent fitted ESR transitions. **c**, Energy level diagram of a two-spin system considering J and D in the presence of B_{ex} and B_{tip}. **d**, Measured (blue dots) and fitted (red curve) ESR splitting Δf of a (3, 4) dimer while rotating the external field by θ with respect to the sample plane. Errors and error bars denote the 95% confidence intervals of the non-linear fits. The total external field $|B_{tot}|$ was kept at 550 mT during the field rotation. All the ESR spectra were taken with the same tip and V = 100 mV. **a** and **b** were obtained with an out-of-plane field of B_z = 550 mT. V_{rf} was set as 50 mV for the centre and right panels of **a** and at 40 mV for those of **b**. ESR spectra of the lower [FePc]$^-$ in each dimer are provided in Supplementary Fig. 4.

note that the ESR peak intensity and linewidth are associated with the spin relaxation time (T_1), spin coherence time (T_2) and driving Rabi rate ($\Omega \propto V_{rf}$). The low bound of T_2 can be extracted by measuring the ESR peak intensity and the linewidth as a function of V_{rf} (ref. [14]), which is approximately 10 ns in our case (Supplementary Section 15).

As shown in Fig. 1c,d, f_0 of a single FePc molecule shifts linearly to lower frequencies as the set tunnelling current (I_{set}) increases at a fixed d.c. bias (V) and B_z, which indicates that B_{tip} is proportional to I_{set} (refs. [26,27]) and opposite to the external magnetic field direction. This holds for all the tips used throughout this article. In Fig. 1d, the vertical intercept, which is determined by extrapolating the curve of f_0 versus I_{set} to zero B_{tip} (I_{set}), corresponds to the Zeeman splitting in the absence of a tip magnetic field. We can thus extract the magnetic moment of an individual [FePc]$^-$ molecule (μ_{FePc}), 1.058 ± 0.003 μ_B, free from the influence of any tip field. For a given tip at each I_{set}, B_{tip} can be calculated precisely by using $B_z - \frac{hf_0}{2\mu_{FePc}}$, where the fitted μ_{FePc} is used, as shown by the two x axes of Fig. 1d. We also found that the magnetic moment extracted from varied external fields at a fixed tip field gave a consistent [FePc]$^-$ magnetic moment of approximately 1 μ_B and obtained an averaged μ_{FePc} of 1.028 ± 0.023 μ_B by measuring 14 individual [FePc]$^-$ molecules (Supplementary Fig. 3). Moreover, we noted that μ_{FePc} differed by approximately 5% in two different directions of the magnetic field (that is, B_x and B_z; Supplementary Fig. 2) and a similar anisotropy in magnetic moment has been found in other systems, for example bulk cobalt phthalocyanine (CoPc) (ref. [28]) and [FePc]$^-$ crystals[29], as verified by standard ESR measurements. This anisotropy results from the spin–orbit coupling that mixes the quenched (L = 0) ground state with excited states of larger orbital moment. The comparison with those bulk

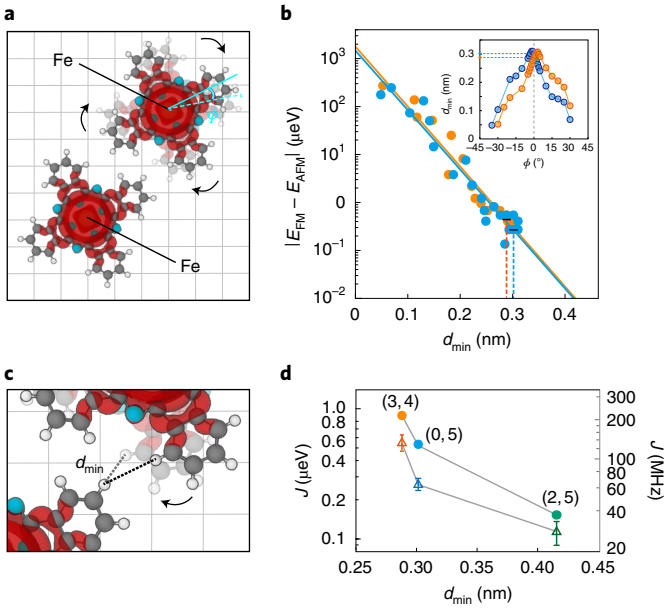

Fig. 3 | DFT calculations of exchange coupling in an [FePc]⁻–[FePc]⁻ dimer atop MgO only. a, Computational model of a [FePc]⁻–[FePc]⁻ dimer. The Fe–Fe distance is set according to experimental Fe coordinates. One molecule is fixed as the other is rotated around the Fe centre by ϕ. The grey grid indicates the MgO lattice. **b**, Calculated energy difference between FM and AFM coupling as a function of d_{min} for (3, 4) (orange dots) and (0, 5) (blue dots) showing a good linearity, which indicates a dominant exchange coupling mechanism. Solid lines are fits based on $|E_{FM} - E_{AFM}| \propto \exp(-d_{min}/d)$. Inset: d_{min} as a function of ϕ. The d_{min} of optimized (3, 4) and (0, 5) configurations and the corresponding $|E_{FM} - E_{AFM}|$ are indicated by dashed lines. **c**, Magnified view of the d_{min} between the two close-by ligands shown in **a**. **d**, Comparison of the calculated (dots) and experimental (triangles) J for three different dimer configurations ((3, 4), orange; (0, 5), blue; (2, 5), green), which showing a very similar trend of J versus d_{min}. The experimental data shown here are only the exchange coupling energy after subtracting D (17 MHz for the (3, 4) and (0, 5) configurations and 14 MHz for the (2, 5) configuration) from $\Delta\bar{f}$. Error bars represent the standard deviation of all the measured coupling energies on each dimer configuration with respect to the mean value (Supplementary Fig. 5). ESR spectra of the (2, 5) dimer are provided in Supplementary Fig. 4.

measurements also shows that the averaged value of the g factor for a single [FePc]⁻ molecule adsorbed on MgO/Ag is smaller and closer to that of a free electron. We note that the difference in g factor between our work on individual [FePc]⁻ molecules and bulk [FePc]⁻ studies may be explained by different local environments (ligand field) and Kondo screening[30,31]. A detailed discussion is provided in Supplementary Section 12. Our results indicate that the magnetic moment of [FePc]⁻ on MgO is weakly anisotropic having spin-1/2 and the tip field can be utilized as a local magnetic field to address an individual spin.

Magnetic interaction between molecules. To investigate the spin–spin interaction of the [FePc]⁻ molecular system, we performed ESR measurements on naturally formed [FePc]⁻–[FePc]⁻ dimers (one such dimer is outlined in white in Fig. 1a). We defined the configuration of a dimer as (m,n) by labelling the separation between the two Fe centres in the dimer in increments of the oxygen lattice along $[01\bar{1}]$ and [011], respectively. We found two dominant configurations, (3, 4) and (0, 5), with identical distances of 1.45 nm (given the MgO lattice constant of 0.29 nm) between the centres of the two molecules. The occurrence of each configuration was approximately 38% and 53%, respectively (Supplementary Fig. 5). When measuring one of the [FePc]⁻ molecules in either dimer (3, 4) or (0, 5), we observed multiple ESR peaks, as shown in Fig. 2a,b, centre panels. For each dimer, the splitting between two adjacent ESR peaks appears to be independent of the tip field, which implies that the splitting is purely associated with the intermolecular coupling, whereas the intensity of each peak evolves differently as the tip field varies (Fig. 2a,b, right panels). Moreover, the ESR splitting on the (3, 4) and (0, 5) dimers was different, although the centre–centre distance was the same in both configurations, which we discuss later.

The two magnetically coupled [FePc]⁻ molecules can be demonstrated by a two-spin system interacting with exchange and dipolar coupling (denoted as parameters J and D, respectively)[32,33]. The corresponding Hamiltonian model is thoroughly discussed in Methods. The presence of exchange and dipolar coupling terms in the two-spin model makes the quantum eigenstates deviate from the four pure Zeeman product states |00>, |01>, |10> and |11>, which gives rise to singlet–triplet states. Although |00> and |11> remain as the eigenstates of the two-spin Hamitonian model, the other two eigenstates become superpositions of the two Zeeman states |01> and |10>, as defined in equation (3):

$$|+> = \frac{1}{\sqrt{\alpha^2+1}}|01> + \frac{\alpha}{\sqrt{\alpha^2+1}}|10>$$
$$|-> = -\frac{\alpha}{\sqrt{\alpha^2+1}}|01> + \frac{1}{\sqrt{\alpha^2+1}}|10>, \quad (3)$$

where α indicates the relative weight o f the |01> and |10> components in the |–> and |+> states[22,32], and is equal to $\frac{\delta+\sqrt{\varepsilon^2+\delta^2}}{\varepsilon}$, in which $\delta = 2(\mu_1 - \mu_2)B_{ex} + 2\mu_1 B_{tip}$ and $\varepsilon = J - \frac{D}{2}(1 - 3\cos^2\theta)$. μ_1 and μ_2 represent the magnetic moments of the [FePc]⁻ molecule under the tip and of the one apart from the tip, respectively. θ is the angle between the unit distance vector $\hat{\mathbf{r}}$ and the [FePc]⁻ spin orientation. Figure 2g depicts a schematic diagram of eigenenergies for the given eigenstates |00>, |–>, |+> and |11> (denoted as E_{00}, E_- E_+ and E_{11}) as a function of B_{ex} and B_{tip}. The four possible transitions between these states account for the ESR peaks shown in Fig. 2a,b (right panels), labelled as $f_1 = \frac{E_- - E_{00}}{h}$, $f_2 = \frac{E_{11} - E_+}{h}$, $f_3 = \frac{E_+ - E_{00}}{h}$, and $f_4 = \frac{E_{11} - E_-}{h}$, respectively. Fitted ESR transitions based on this singlet–triplet model (dotted white curves in Fig. 2a,b, right panels) show excellent agreement with the experimental data (Supplementary Section 5).

From the expression of α with δ, we note that the tip field can tune the relative weight of |01> and |10>in the |–> and |+> states at a given B_{ex}, which leads to different dominant ESR transitions at different tip fields (bold arrows in Fig. 2c at the weak and strong tip fields). This accounts for the changes in the relative peak intensities of the four ESR transitions. In particular, when B_{tip} is adjusted to achieve $\delta = 0$ (which occurs at the avoided level crossing indicated by the dashed square in Fig. 2c) and $\alpha = 1$, meaning B_{tip} compensates the difference in the Zeeman energy of the two [FePc]⁻ spins (which originates from the unequal magnetic moments), |10> and |01> are equally weighted in |–> and |+>, f_1 and f_4 have the same intensity and f_2 and f_3 merge to one peak (when $D \ll J$ and thus negligible), as indicated by the white arrows in Fig. 2a,b (right panels).

Using the above Hamiltonian model, we found that the ESR splitting Δf ($\Delta f = f_2 - f_1 = f_4 - f_3$) corresponds to the total coupling energy of the two-spin system:

$$\Delta f = J + D\left(1 - 3\cos^2\theta\right). \quad (4)$$

Here, Δf depends on the angle between the external field and the sample plane due to an anisotropic dipolar distribution. We recorded

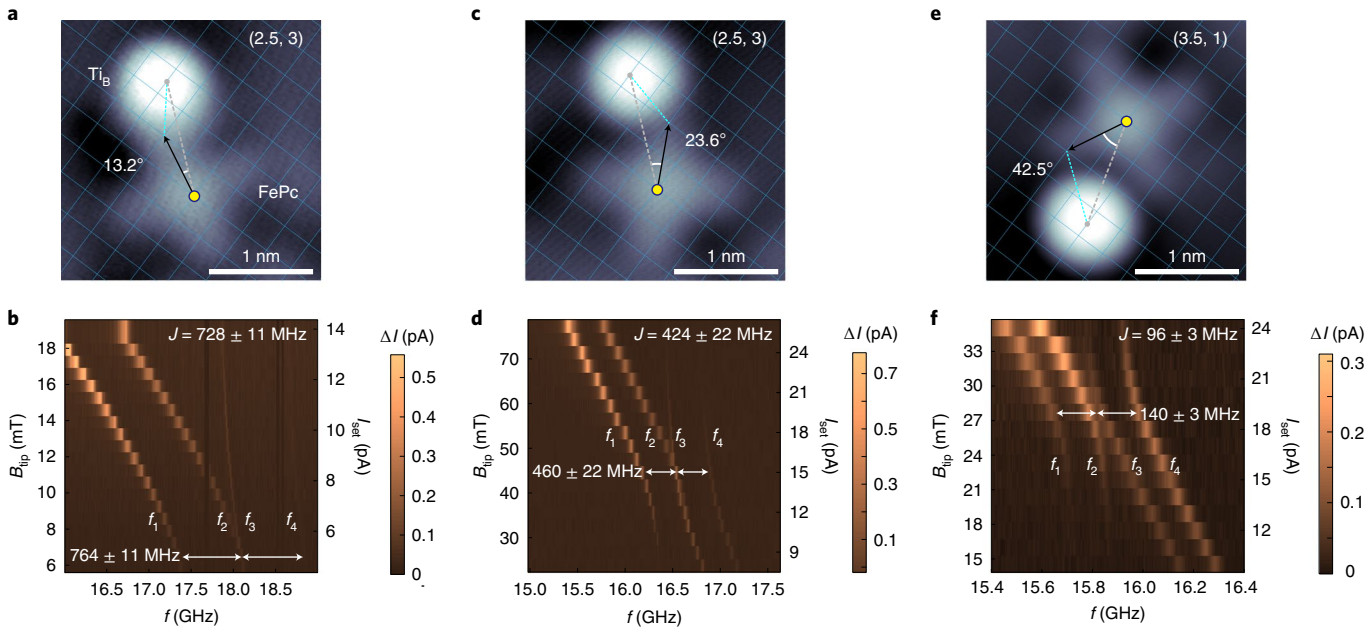

Fig. 4 | Exchange coupling of [FePc]$^-$–Ti$_B$ pairs with different Ti$_B$–ligand distance. a,**b**, [FePc]$^-$–Ti$_B$ pair with a (2.5, 3) configuration. **c**,**d**, A second pair in a (2.5, 3) configuration. **e**,**f**, A pair in a (3.5, 1) configuration. The three pairs have similar Fe–Ti$_B$ distances, but different angles between molecular axes and the connection of Fe–Ti$_B$. **a**,**c**,**e**, STM images of the three pairs. Scanning conditions: $V = 200$ mV, $I_{set} = 6$ pA (**a**); $V = 200$ mV, $I_{set} = 10$ pA (**c**); $V = 150$ mV, $I_{set} = 20$ pA (**e**). The blue grids indicate oxygen sites of the underlying MgO surface. **b**,**d**,**f**, Respective ESR spectra measured on [FePc]$^-$ (yellow spots in **a**, **c** and **e**, respectively) as a function of tip field by varying the set point of the tunnelling current. J of each [FePc]$^-$–Ti$_B$ pair is given on the upper right corner, obtained by subtracting the dipolar coupling contribution (36 MHz for the (2.5, 3) pairs and 44 MHz for the (3.5, 1) pair) from the measured ESR splitting. The significant change in J when Ti$_B$ is positioned at different sites with respect to the molecular ligands implies a molecular-geometry-depended exchange interaction. The errors were obtained from the 95% confidence intervals of the non-linear fits. The external magnetic field was along the out-of-plane direction for all [FePc]$^-$–Ti$_B$ measurements in our work. ESR conditions: $V = 100$ mV for all three pairs and $V_{rf} = 30$ mV, $B_z = 650$ mT (), $V_{rf} = 10$ mV, $B_z = 600$ mT (**d**) and $V_{rf} = 30$ mV, $B_z = 570$ mT (**e**).

Δf measured on a (3, 4) dimer with rotating external fields to differentiate the magnetic dipole interaction from the exchange interaction, as shown in Fig. 2d. By fitting to equation (4), we extracted J and D as 133 ± 4 MHz and 16 ± 3 MHz, respectively, which strongly suggests that the exchange coupling is the dominant interaction in the molecular spin pairs. The positive sign of J indicates that the coupling is antiferromagnetic (AFM). Moreover, we note that the measured D here is consistent with that expected from two ideal atomic spins having $1\,\mu_B$ with same centre–centre distance[22,32,33]. Based on this, we can extract the exchange coupling energy (J) of [FePc]$^-$ dimers by subtracting D of an atomic dimer with same centre–centre distance from the measured ESR splitting (Δf).

Previous ESR–STM studies on spin–spin interaction for atomic spins showed that the exchange coupling is determined exclusively by the interatomic distance, which implies that the atomic spin can be treated as a point magnet[22,32,33]. However, we found that the exchange coupling energies of the (3, 4) and (0, 5) molecular dimers are different despite having the same centre–centre distance. By measuring the ESR splitting (Δf) of approximately 30 dimers with the B_z field only, we obtained a mean $\overline{\Delta f}$ of 134 ± 19 MHz for the (3, 4) dimer and of 64 ± 7 MHz for the (0, 5) dimer (Supplementary Fig. 5). As mentioned above, the corresponding J extracted from $\overline{\Delta f}$ is 117 ± 19 MHz and 47 ± 7 MHz, respectively, by subtracting a dipole contribution of 17 MHz (calculated with two atomic spins of $1\,\mu_B$ each). The non-negligible spin density on the Pc ligands may produce such a difference by generating an additional coupling path for the intermolecular magnetic interaction. This implies that the distance between nearby ligands plays a crucial role in determining the magnetic coupling energy of molecular spin systems.

DFT model. We performed DFT calculations to evaluate the influence of the ligand–ligand distance on the exchange coupling energy of [FePc]$^-$ dimers. For both (3, 4) and (5, 0) dimers, the optimized adsorption configuration on a MgO surface was achieved when the two Fe centres were atop oxygen sites and the molecular lobes aligned along the (2, 1) lattice direction, in good agreement with our STM topographic images displayed in Fig. 2a,b (left panels). In subsequent calculations, we fixed one molecule in its optimized configuration (lower one in Fig. 3a) while rotating the other molecule (upper one in Fig. 3a) around its Fe centre by an angle ϕ with respect to the (2, 1) lattice direction. The centre–centre distance remained unchanged during such a rotation, and the minimal ligand–ligand distance d_{min} (defined as the nearest distance between two hydrogen atoms in the benzene rings, as shown in Fig. 3c) changed accordingly. The variation in d_{min} when ϕ changes in the (3, 4) and (5, 0) configurations is exhibited in the inset of Fig. 3b. We note a small difference in the d_{min} of the (3, 4) and (5, 0) dimers when they are in the optimized configurations (that is, $\phi = 0°$). We then calculated the energy difference between the ferromagnetic (E_{FM}) and the AFM (E_{AFM}), the value of which equals to $\frac{1}{2}J$ for a two spin-1/2 system[34], as a function of d_{min} (Fig. 3b). The calculated $|E_{FM} - E_{AFM}|$ obeys an exponential decay ($\propto \exp(-d_{min}/d)$) as d_{min} increases, which can be attributed to an exchange interaction through the ligands. We extracted a characteristic decay length of $d = 0.0345$ nm, which is similar to the length scale of exchange coupling in other molecular systems[35]. In our calculations, we note that the exchange coupling energy only differs slightly with and without an MgO substrate, which implies the negligible role of the substrate in the intermolecular interaction. Notably, the exchange interaction between two molecular spins is mediated through the fully occupied orbit-

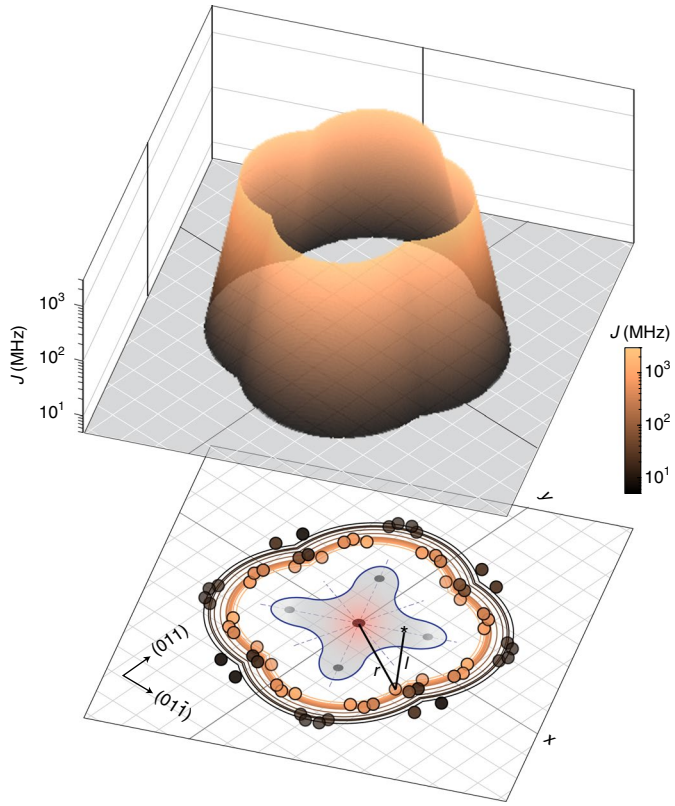

Fig. 5 | Molecular-geometry-dependent exchange coupling in $[FePc]^-$–Ti_B pairs. Lower panel: measured *J* of different $[FePc]^-$–Ti_B pairs expressed by coloured dots and labelled at the corresponding Ti_B adsorption sites with respect to the central $[FePc]^-$ model. In total, 14 pairs were measured and the data points that correspond to the measured *J* were equivalently duplicated by a rotation and reflection process according to the molecular symmetry axes (dashed lines). The grey grids represent the oxygen lattice. *J* is the exchange coupling energy after subtracting the dipole contribution from the total ESR splitting. The contour lines are projected from the simulated spatial exchange coupling energy map choosing those *J* values obtained from the experiment. Upper panel: simulated spatial exchange coupling energy map using the sum of two exponential terms which represent the *r* dependence and *l* dependence. The simulated results are in good agreement with the experimental data, which unveils the geometry dependence of the exchange coupling with a molecule. The frequency range used in the simulation was set as 3,000 MHz (upper limit) and 5 MHz (lower limit).

als of the ligand, which suggests a superexchange mechanism (see Supplementary Section 14 for a detailed discussion). The calculated *J* decreases as d_{min} becomes larger in the optimized (3, 4), (0, 5) and (2, 5) dimer configurations, consistent with the trend observed in our experiments (Fig. 3d). Besides, we found a few dimers whose ligand–ligand distance (Supplementary Fig. 7) deviated apparently from the optimized dimer configurations. The exchange coupling energy was significantly larger at equal centre–centre distances but shorter ligand–ligand distances. This result indicates that the molecular spin–spin coupling can be engineered via tuning inter-ligand symmetry.

Sensing molecular spin distribution. To sense the spin distribution on the Pc ligands in greater detail, we substituted a spin-1/2 Ti_B atom for a $[FePc]^-$ molecule and measured the exchange coupling energy in $[FePc]^-$–Ti_B pairs. Although $[FePc]^-$ dimers prefer to arrange only in a few configurations, as mentioned above, the relative spatial position of a Ti_B atom with respect to a $[FePc]^-$ molecule can be controlled with atomic precision using atom manipulation. Here, the Ti_B atom is considered as a point magnet, based on previous studies[32,33] and our DFT calculations (Supplementary Fig. 10). We applied only a B_z field to measure $[FePc]^-$–Ti_B pairs to be able to ignore the angular dependence of the dipolar interaction. The measured exchange coupling energy was thus merely its component along the out-of-plane direction, simplified as *J*. Figure 4a,c,e shows three $[FePc]^-$–Ti_B pairs with the Ti_B atom sitting on different lattice sites: (2.5, 3), (2.5, 3) and (3.5, 1) with similar centre–centre (Fe–Ti_B) distances of 1.13, 1.13 and 1.06 nm. However, the relative angle between the connection of Fe–Ti_B and the molecular axes varies from 13.2 to 42.5°, which correspond to different Ti_B–ligand distances. As the angle became larger, that is, the Ti_B is further away from the closest $[FePc]^-$ ligand, we observed a drastic decrease in *J* by measuring ESR on $[FePc]^-$, as exhibited in Fig. 4b,d,f. Referring to the $[FePc]^-$– $[FePc]^-$ dimer case, the *J* values shown here are the result after subtracting *D* from Δf. The strong dependence on the relative Ti_B–ligand configuration of the exchange coupling energy indicates that the ligands can influence the magnetic interaction dramatically, which agrees with our measurements on $[FePc]^-$–$[FePc]^-$ dimers.

To map the molecular-geometry-dependent spin distribution of the $[FePc]^-$ molecules, we measured *J* of a total of 14 $[FePc]^-$–Ti_B pairs and observed a drastic decay of *J* as both Fe–Ti_B distance (*r*) and ligand–Ti_B distance (*l*) increases (Supplementary Fig. 8). Figure 5 (lower panel) displays the spatial map of *J* measured in different $[FePc]^-$–Ti_B pairs. Considering the D_{4h} symmetry of the $[FePc]^-$ molecule with respect to the MgO lattice, we duplicated the *J* of each pair to those equivalent adsorption sites. To emphasize the spin distribution on both the Fe centre and the Pc ligands, we utilized a heuristic model that simplified the entire spin distribution as two spin centres sitting at the central Fe atom and the nearest ligand, respectively. In this model, the *J* of a $[FePc]^-$–Ti_B pair with the Ti_B sitting at (*r*,*l*) with respect to the molecule can be described by the sum of two exponential functions, $J(r,l) = J_0(c_1 \cdot e^{-r/\lambda} + c_2 \cdot e^{-l/\lambda})$. Here, J_0 is the exchange coupling energy constant, which is assumed to be the same for the Fe–Ti_B and ligand–Ti_B interactions. c_1 and c_2 are fitting prefactors. λ is the characteristic decay length towards the molecular centre (Fe) and the ligand centre, respectively. By choosing different lattice sites along the (2, 1) direction to determine *l* in the fitting, we note that c_1 and c_2 are optimized when the reference spot on the ligand is set at (1.42, 0.71), which gives a ratio of $\frac{c_2}{c_1} = 0.03$, consistent with the <30% contribution of the spin density from the ligands (<7% for each ligand). The characteristic decay length is fitted as $\lambda = 0.0506$ nm (see Supplementary Information Section 7 for more details). This allows us to approximate the spatial distribution of the exchange interaction with a molecule when the Ti_B spin is positioned at different sites, as shown in the upper panel of Fig. 5. We found good agreement between this simple model and the experimental data by comparing the simulated contour lines with those measured data points, which revealed the molecular-geometry dependence of an exchange interaction with a molecular spin. These results highlight that ligands play a crucial role in molecular spin–spin interactions.

Conclusion

In conclusion, we have demonstrated single-molecule ESR by driving the spin of an individual $[FePc]^-$ molecule on a surface. ESR–STM measurements on molecular dimers and molecule–metal atom pairs enabled us to investigate the crucial role of the Pc ligands on the exchange coupling between $[FePc]^-$ molecules. The spin–spin interaction energy that we measured is only in the hundreds of megahertz range (~100 neV) and the measurement of the spin coherence time allows the molecular spin to be one of potential candidates for molecular quantum control experiments. Most importantly, we found that the magnetic exchange interaction with a molecule shows a strong dependence on molecular geometry, which emphasizes the important role of ligands for the transfer

of spin polarization in molecular systems. Our work extends ESR–STM from single atoms to a much larger class of matter—magnetic molecules. This allows synthetic chemistry to design the spin properties through engineering the ligand field and symmetry. In addition, one can utilize ESR-active atoms or molecules to detect the spin distribution of other general molecular systems via dipolar and exchange interactions. Our work suggests molecules as a potential platform to investigate magnetic interactions with non-localized spins, which has brought intensive interest in the field of coordination networks and is essential to develop molecule-based spintronic and quantum information devices[36].

Online content

Any methods, additional references, Nature Research reporting summaries, source data, extended data, supplementary information, acknowledgements, peer review information; details of author contributions and competing interests; and statements of data and code availability are available at https://doi.org/10.1038/s41557-021-00827-7.

Received: 22 December 2020; Accepted: 27 September 2021;
Published online: 11 November 2021

References

1. Atzori, M. & Sessoli, R. The second quantum revolution: role and challenges of molecular chemistry. *J. Am. Chem. Soc.* **141**, 11339–11352 (2019).
2. Wrachtrup, J., von Borczyskowski, C., Bernard, J., Orrit, M. & Brown, R. Optical detection of magnetic resonance in a single molecule. *Nature* **363**, 244–245 (1993).
3. Köhler, J. et al. Magnetic resonance of a single molecular spin. *Nature* **363**, 242–244 (1993).
4. Bayliss, S. L. et al. Optically addressable molecular spins for quantum information processing. *Science* **370**, 1309–1312 (2020).
5. Rugar, D., Budakian, R., Mamin, H. J. & Chui, B. W. Single spin detection by magnetic resonance force microscopy. *Nature* **430**, 329–332 (2004).
6. Lovchinsky, I. et al. Nuclear magnetic resonance detection and spectroscopy of single proteins using quantum logic. *Science* **351**, 836–841 (2016).
7. Gehring, P., Thijssen, J. M. & van der Zant, H. S. J. Single-molecule quantum-transport phenomena in break junctions. *Nat. Rev. Phys.* **1**, 381–396 (2019).
8. Vincent, R., Klyatskaya, S., Ruben, M., Wernsdorfer, W. & Balestro, F. Electronic read-out of a single nuclear spin using a molecular spin transistor. *Nature* **488**, 357–360 (2012).
9. Thiele, S. et al. Electrically driven nuclear spin resonance in single-molecule magnets. *Science* **344**, 1135–1138 (2014).
10. Tesi, L. et al. Quantum coherence in a processable vanadyl complex: new tools for the search of molecular spin qubits. *Chem. Sci.* **7**, 2074–2083 (2016).
11. Graham, M. J. et al. Influence of electronic spin and spin–orbit coupling on decoherence in mononuclear transition metal complexes. *J. Am. Chem. Soc.* **136**, 7623–7626 (2014).
12. Seifert, T. S. et al. Single-atom electron paramagnetic resonance in a scanning tunneling microscope driven by a radio-frequency antenna at 4 K. *Phys. Rev. Res.* **2**, 013032 (2020).
13. Natterer, F. D. et al. Upgrade of a low-temperature scanning tunneling microscope for electron-spin resonance. *Rev. Sci. Instrum.* **90**, 013706 (2019).
14. Baumann, S. et al. Electron paramagnetic resonance of individual atoms on a surface. *Science* **350**, 417–420 (2015).
15. Willke, P. et al. Hyperfine interaction of individual atoms on a surface. *Science* **362**, 336–339 (2018).
16. Yang, K. et al. Electrically controlled nuclear polarization of individual atoms. *Nat. Nanotechnol.* **13**, 1120–1125 (2018).
17. Durkan, C. & Welland, M. E. Electronic spin detection in molecules using scanning-tunneling-microscopy-assisted electron-spin resonance. *Appl. Phys. Lett.* **80**, 458–460 (2002).
18. Hiraoka, R. et al. Single-molecule quantum dot as a Kondo simulator. *Nat. Commun.* **8**, 16012 (2017).
19. Mugarza, A. et al. Electronic and magnetic properties of molecule–metal interfaces: transition-metal phthalocyanines adsorbed on Ag(100). *Phys. Rev. B* **85**, 155437 (2012).
20. Yang, K. et al. Tunable giant magnetoresistance in a single-molecule junction. *Nat. Commun.* **10**, 3599 (2019).
21. Bogani, L. & Wernsdorfer, W. Molecular spintronics using single-molecule magnets. *Nat. Mater.* **7**, 179–186 (2008).
22. Bae, Y. et al. Enhanced quantum coherence in exchange coupled spins via singlet-triplet transitions. *Sci. Adv.* **4**, eaau4159 (2018).
23. Willke, P., Yang, K., Bae, Y., Heinrich, A. J. & Lutz, C. P. Magnetic resonance imaging of single atoms on a surface. *Nat. Phys.* **15**, 1005–1010 (2019).
24. Tsukahara, N. et al. Adsorption-induced switching of magnetic anisotropy in a single iron(II) phthalocyanine molecule on an oxidized Cu(110) surface. *Phys. Rev. Lett.* **102**, 167203 (2009).
25. Abragam, A. & Bleaney, B. *Electron Paramagnetic Resonance of Transition Ions* (Oxford Univ. Press, 2012).
26. Yang, K. et al. Tuning the exchange bias on a single atom from 1 mT to 10 T. *Phys. Rev. Lett.* **122**, 227203 (2019).
27. Yan, S., Choi, D.-J., Burgess, J. A. J., Rolf-Pissarczyk, S. & Loth, S. Control of quantum magnets by atomic exchange bias. *Nat. Nanotechnol.* **10**, 40–45 (2015).
28. Assour, J. M. & Kahn, W. K. Electron spin resonance of α- and β-cobalt phthalocyanine. *J. Am. Chem. Soc.* **87**, 207–212 (1965).
29. Konarev, D. V. et al. Ionic compound containing iron phthalocyanine $(Fe^{I}Pc)^{-}$ anions and $(C_{70}^{-})_2$ dimers. Optical and magnetic properties of $(Fe^{I}Pc)^{-}$ in the solid state. *Dalton Trans.* **41**, 13841–13847 (2012).
30. Wolf, E. L. & Losee, D. L. G-shifts in the 's-d' exchange theory of zero-bias tunneling anomalies. *Phys. Lett. A* **29**, 334–335 (1969)
31. Barnes, S. E. Theory of electron spin resonance of magnetic ions in metals. *Adv. Phys.* **30**, 801–938 (1981).
32. Yang, K. et al. Engineering the eigenstates of coupled spin-1/2 atoms on a surface. *Phys. Rev. Lett.* **119**, 227206 (2017).
33. Choi, T. et al. Atomic-scale sensing of the magnetic dipolar field from single atoms. *Nat. Nanotechnol.* **12**, 420–424 (2017).
34. Noodleman, L. Valence bond description of antiferromagnetic coupling in transition metal dimers. *J. Chem. Phys.* **74**, 5737–5743 (1981).
35. Czap, G. et al. Probing and imaging spin interactions with a magnetic single-molecule sensor. *Science* **364**, 670–673 (2019).
36. Ferrando-Soria, J. et al. A modular design of molecular qubits to implement universal quantum gates. *Nat. Commun.* **7**, 11377 (2016).
37. Zhang, X. et al. Electron spin resonance of single iron-phthalocyanine molecules and role of their non-localized spins in magnetic interaction (source data, codes and raw images). *Figshare* https://doi.org/10.6084/m9.figshare.16574534.v1 (2021).

Methods

STM-ESR set-up. ESR measurements were performed in a commercial low-temperature STM (Unisoku, USM1300). A radio frequency microwave, generated by a signal generator (Keysight, E8257D), was added to a d.c. voltage using a bias tee at the tip side. With this set-up, an oscillating electric field V_{rf} was applied at the tunnelling junction. The magnetic tip was prepared by transferring about 3–5 Fe atoms from the MgO surface to the tip apex, which allowed a readout of the spin state by the spin-polarized tunnelling current. During an ESR frequency sweep, the radio frequency voltage and d.c. bias were applied continuously, but the radio frequency voltage was modulated at 95 Hz. The modulated tunnelling current was then recorded by a lock-in technique. All the voltages in this article are referred to the sample.

Sample preparation. In our work, all the materials used for sample preparation were commercially purchased. Single-crystalline Ag(100) was purchased from MaTek. FePc was purchased from Sigma-Aldrich with a purity of 90%. Highly pure Fe and Ti rods (99.95%) were purchased from Goodfellow. Mg in dendritic pieces was purchased from Sigma-Aldrich with a purity of 99.998%. The O_2 (99.995%) used here was supplied by a local vendor. The Ag(100) substrate was pretreated by alternating Ar^+ sputtering and annealing cycles. During the MgO growth, Ag(100) was kept at 400 °C and magnesium was evaporated onto clean Ag surface in an O_2 atmosphere of 1.1×10^{-6} torr. FePc was first deposited onto the MgO surface with the sample kept at room temperature. The sample was then transferred to the cryostat to cool down. Fe and Ti atoms were deposited subsequently onto the cold sample at 25–40 K. After the dosage of molecules and metal atoms, the sample was transferred to ~2 K environment for ESR measurements. The thickness of the MgO film was determined by performing point-contact measurements on individual Fe atoms[38] and varied from 2 to 4 ML in our case. Our measurements were all performed on a 2 ML MgO. Also, we note that the MgO patches were found to be surrounded with large irregular Ag terraces. A detailed discussion on the sample morphology is provided in Supplementary Section 9.

All the STM images displayed in this work were processed by WSxM[39] in the 'Bone' colour mode. A low-order Gaussian filtering function was applied to the images for a better visual effect without hindering the authenticity. The original STM files and unprocessed images can be found in Zhang et al.[37]. All the ESR spectra plotted in a colour scale were dealt with the 'Copper' colour mode.

Titanium atom manipulation. After titanium deposition, naturally formed $[FePc]^-$–Ti_B pairs were abundant. In addition, we were able to position the Ti_B atom using atom manipulation and construct $[FePc]^-$–Ti_B pairs with various configurations. When the tunnelling conductance was set as $V\approx350$ mV, $I_{set}\approx2.2$ nA, the Ti_B atom under the tip could follow the tip movement and be positioned at the desired sites. In contrast, controllable manipulation of a $[FePc]^-$ molecule rarely occurs under our manipulation parameters.

Hamiltonian model of the two-molecule system. To understand the ESR spectra quantitatively, we used a Hamiltonian model of the two-spin system, which included exchange and dipolar coupling[32,33] between two $[FePc]^-$ molecules:

$$H_{12} = 2\mu_1\left(\mathbf{B}_{ex}+\mathbf{B}_{tip}\right)\cdot\mathbf{S}_1+2\mu_2\mathbf{B}_{ex}\cdot\mathbf{S}_2 + J\mathbf{S}_1\cdot\mathbf{S}_2+D[\mathbf{S}_1\cdot\mathbf{S}_2-3(\mathbf{S}_1\cdot\hat{\mathbf{r}})(\mathbf{S}_2\cdot\hat{\mathbf{r}})]. \quad (5)$$

Here, the subscripts 1, and 2 represent the two $[FePc]^-$ spins in a dimer. The one under the tip is denoted as 1, whose Zeeman energy is set by both $\mathbf{B}_{ex}$ and $\mathbf{B}_{tip}$. $\mathbf{S}_1$ and $\mathbf{S}_2$ are the spin operators of the two molecular spins. The first two terms describe the Zeeman energy of a dimer system. Both $[FePc]^-$ spins align with the external magnetic field direction as both molecules are spin-1/2. The third and last terms represent the intermolecular exchange and dipolar coupling with the energy constants J and D, respectively. $\hat{\mathbf{r}}$ is the unit distance vector that connects the centres of two FePc spins. D is given by $\frac{\mu_0\mu_1\mu_2}{\pi r^3}$, where μ_0 is the vacuum permeability.

DFT calculations. All the DFT calculations were performed using Quantum Espresso (version 6.5) which implements DFT using plane waves and pseudopotentials[40,41]. Pseudopotentials were chosen based on the SSSP library, and the basis set was expanded using a kinetic cutoff of 40 Ry (ref. [42]). All the pseudopotentials use the generalized Perdew–Burke–Ernzerhof gradient approximation and we treated van der Waals interactions using Grimme's D3[43,44]. For a single FePc, the calculation model included 4 ML of silver capped by 2 ML of MgO with the (100) surface exposed. In the z direction, the cell was padded with 1.2 nm of vacuum. For the $[FePc]^-$–$[FePc]^-$ dimer, the cell was laterally expanded to accommodate both molecules and make sure that the separation of the dimers and their periodic image was at least five times larger than the interdimer distance. The exchange coupling energy was calculated using the broken-symmetry approach introduced by Noodleman[34]. This approach maps the Kohn–Sham energies of the high-spin ($m_s=1$) and broken symmetry ($m_s=0$) states to the diagonal elements of the Heisenberg Hamiltonian. More computational details can be found in the Supplementary Information. The computational models are provided as additional supplementary files and also available in Zhang et al.[37].

Data availability

All the data that support the findings of this study are available in this article and its Supplementary Information, or from the corresponding authors on reasonable request. The source data and DFT models that support all the figures displayed in the main article and Supplementary Information are also publicly available through the link https://doi.org/10.6084/m9.figshare.16574534.v1[37].

Code availability

The MATLAB code used to plot and fit the ESR spectra displayed in article and Supplementary Information is available through the Figshare link, https://doi.org/10.6084/m9.figshare.16574534.v1[37]. WSxM software[39] was used to change the colour schemes of our STM images for better clarity; we used the integrated low-order Gaussian filtering function, a built-in function within the software, without modifications.

References

38. Paul, W. et al. Control of the millisecond spin lifetime of an electrically probed atom. *Nat. Phys.* **13**, 403–407 (2017).
39. Horcas, I. et al. WSXM: a software for scanning probe microscopy and a tool for nanotechnology. *Rev. Sci. Instrum.* **78**, 013705 (2007).
40. Giannozzi, P. et al. QUANTUM ESPRESSO: a modular and open-source software project for quantum simulations of materials. *J. Phys. Condens. Matter* **21**, 395502 (2009).
41. Giannozzi, P. et al. Advanced capabilities for materials modelling with Quantum ESPRESSO. *J. Phys. Condens. Matter* **29**, 465901 (2017).
42. Prandini, G., Marrazzo, A., Castelli, I. E., Mounet, N. & Marzari, N. Precision and efficiency in solid-state pseudopotential calculations. *npj Comput. Mater.* **4**, 1–17 (2018).
43. Perdew, J. P., Burke, K. & Ernzerhof, M. Generalized gradient approximation made simple. *Phys. Rev. Lett.* **77**, 3865–3868 (1996).
44. Grimme, S., Hansen, A., Brandenburg, J. G. & Bannwarth, C. Dispersion-corrected mean-field electronic structure methods. *Chem. Rev.* **116**, 5105–5154 (2016).

Acknowledgements

All the authors acknowledge support from the Institute for Basic Science under grant IBS-R027-D1. P.W. also acknowledges funding from the Emmy Noether Programme of the DFG (WI5486/1-1). We thank N. Lorente for fruitful discussions.

Author contributions

T.C. and X.Z. designed the project. X.Z., Y.W., T.B. and P.W. performed the experiments. C.W. carried out the DFT calculations. H.A. contributed to the Hamiltonian model simulations. X.Z. and T.C. wrote the manuscript with the help of all the authors. T.C. and A.J.H. advised the project process.

Competing interests

The authors declare no competing interests.

Additional information

Supplementary information The online version contains supplementary material available at https://doi.org/10.1038/s41557-021-00827-7.

Correspondence and requests for materials should be addressed to Andreas J. Heinrich or Taeyoung Choi.

Peer review information *Nature Chemistry* thanks the anonymous reviewers for their contribution to the peer review of this work.